Plasma Sources Sci. Technol. **18** (2009) 045004 (13pp) doi:10.1088/0963-0252/18/4/045004

Experimental study of plasma parameters in a vacuum arc with a hot refractory anode

A Shashurin, I I Beilis and R L Boxman

Electrical Discharge and Plasma Laboratory, School of Electrical Engineering,
Fleischman Faculty of Engineering, Tel Aviv University, PO Box 39040, Tel Aviv 69978, Isreal

Received 9 December 2008, in final form 28 June 2009
Published 31 July 2009
Online at stacks.iop.org/PSST/18/045004

Abstract
The spatial distributions of plasma density, electron temperature, plasma potential and ion energy were measured during hot refractory anode vacuum arc (HRAVA) development as functions of arc current and inter-lectrode gap distance. Plasma density increased with arc time and saturated ($\geqslant 10^{14}$ cm^{-3}) in the developed HRAVA stage. While the ion energy in the anode plasma at the gap exit was relatively small, the ions were accelerated outside the gap in radially expanding plasma to ~15 eV at 19 cm from the electrode axis. The electron temperature decreased during anode plume development and was $\geqslant 1$ eV in the developed HRAVA stage. Measured plasma parameters agreed well with previously developed theory.

(Some figures in this article are in colour only in the electronic version)

1. Introduction

Presently, plasma generated by cathodic vacuum arcs is used for surface treatment, implantation and thin film deposition [1]. In the cathodic arc, plasma jets, comprising vaporized and ionized cathode material, are generated. The main disadvantage of cathodic plasma jets for practical applications is the presence of large numbers of macroparticles (MPs)—droplets of the cathode material with characteristic sizes varying from sub-micrometer up to hundreds of micrometers. Presently, there are two main methods for depositing MP-free thin films using the vacuum arc: filtering the MPs from the cathode jets using magnetic filters and utilization of arc modes where MP generation is repressed (e.g. the hot anode vacuum arc).

A relatively new method in the second category using a hot anode is called the hot refractory anode vacuum arc (HRAVA) [2]. The HRAVA is ignited between a cooled cathode and a thermally isolated refractory anode (for example from molybdenum or graphite). Initially the discharge operates in the conventional cathodic arc mode and produces cathodic plasma jets. During this stage cathode plasma jets deposit cathode material on the anode surface, while the anode is heated by the arc. A dense anode plasma plume forms when the anode becomes sufficiently hot to re-evaporate the deposited cathode material from the anode surface. This material is ionized in the oncoming plasma jets, expands radially into the ambient vacuum and may be used to deposit films with strongly reduced MP contamination in comparison with that obtained using cathodic arcs.

Some of the HRAVA plasma parameters were experimentally determined previously [3–6]. The temporal and spatial distributions of the plasma density and electron temperature in the inter-electrode space were measured [3] during the first minute of arcing. The electron temperature initially was about 1.6 eV and decreased to about 1.1 eV after 20 s (in the center of a 1 cm gap in a 340 A arc). The radial energy flux generated by 175 and 340 A Cu arcs was about 1 MW m^{-2} and 2 MW m^{-2}, respectively, at the edge of the inter-electrode space. The ion energy distribution, plasma density and electron temperature were measured in the radially expanding plasma of the HRAVA during the first 20 s of arcing and $I_{arc} = 175$ A [4, 5]. The peak of the ion energy distribution shifted to higher energies with an increase in the distance from the electrode axis, 8–20 eV for 3–18 cm. This ion acceleration was explained by the large plasma density gradient in the expanding plasma. In the same radial distance range, the electron temperature decreased from 1.2 to 0.6 eV, the plasma potential decreased from 3.7 to 1.7 V with respect to the grounded anode and the plasma density decreased from 2×10^{13} to 2×10^{11} cm^{-3}. The inter-electrode HRAVA plasma with a graphite anode was analyzed spectroscopically [6], and

lines of Cu I, Cu II and Cu III were observed, while spectral lines of the anode material were not found.

A theoretical model of the HRAVA was formulated by Beilis *et al* [2, 7, 8]. The model considered the following physical processes: evaporation of cathode material from the anode surface, 1D gas-dynamics in the gap filled by cathode vapor; ionization of re-evaporated flux by cathode jets, plasma expansion inside and outside the gap, balances of energy and particle number in the gap and 1D nonlinear heat flow in the anode during heating by the inter-electrode plasma. The temporal evolution of the plasma density, electron temperature, ion energy, heat fluxes to the arc electrodes and surroundings, anode temperature and effective anode potential were calculated. Steady state was predicted, e.g. plasma parameters in 175 A arc were calculated to reach steady state in times $t \geqslant 1$ min [2]. During steady state, the model predicted radial plasma acceleration in the electron pressure gradient, anode heating to temperatures >2000 K and plasma electron temperatures of ∼1 eV.

However, plasma parameters outside the gap (plasma density, electron temperature, ion energies) were measured only for $t = 20$ s [4, 5], but not for longer times. Analogously the inter-electrode plasma parameters (plasma density and electron temperature) were determined for the first minute of arcing [3], but not for longer times, and thus not under steady-state conditions [2], while this mode is of interest both for theoretical [2] and practical reasons. The objective of this work was to determine the plasma parameters including plasma density, electron temperature and ion energies, both inside and outside the gap, for different arc currents, inter-electrode gaps and anode materials, in a long duration HRAVA.

2. Experimental details and methodology

Experimental apparatus. Experiments were conducted in a cylindrical vacuum chamber (400 mm length, 160 mm diameter) shown in figure 1. The chamber was pumped by a diffusion pump to 2×10^{-5} Torr (2.66×10^{-3} Pa). Arcing was initiated using mechanical trigger between a water-cooled copper cathode (diameter $D_c = 30$ mm) and Mo or graphite (POCO DFP-1) anodes (diameter $D_a = 32$ mm and length 30 mm). Arc currents were $I_{arc} = 175$–340 A, and the inter-electrode gap was $h \leqslant 10$ mm.

Plasma density (n_e), electron temperature (T_e), plasma potential (U_{pl}) and floating potential (U_{fl}) were determined using single, triple and emissive probes, while ion energy was measured using a retarding field analyzer (RFA).

Triple probe. A triple probe [5, 9] comprised three tungsten wires (diameter $D_w = 0.5$ mm) within a boron nitride (BN) tube (3.5 mm diameter). The wires were placed at the vertices of an equilateral triangle with sides of about 1 mm. Constant voltage $U_{dc} = 18$ V was applied between wires 1 and 2 (negative potential to the wire 1) as shown in figure 2(*a*). Since the electron temperature T_e did not exceed a few electronvolts, an ordinary double probe formed by wires (1–2) collected ion saturation current I_{is}. The potential drop (U_1) on a small shunt resistor R_1 was measured and I_{is} was determined as

$$I_{is} = U_1/R_1. \tag{1}$$

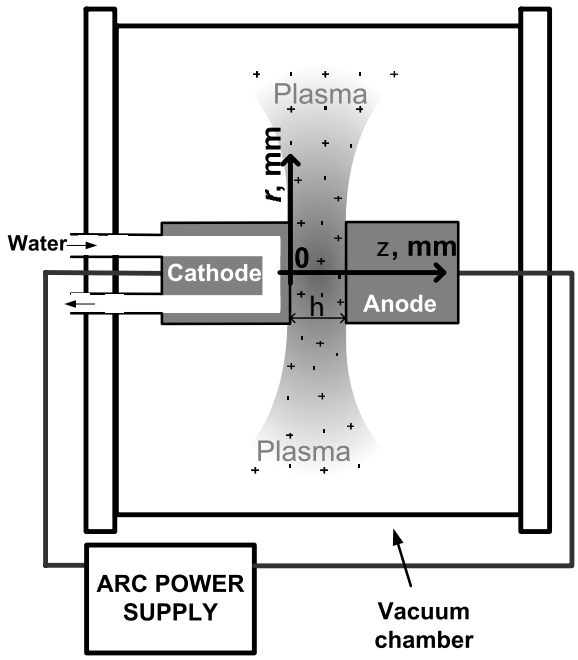

Figure 1. Schematic diagram of the experimental setup and the coordinate system.

Wire 3 was floating; its potentials with respect to wire 2 (U_{2-3}) and to the grounded anode–floating potential (U_{fl}) were measured. The electron temperature was determined from U_{2-3} as follows [9]:

$$T_e = \frac{U_{2-3}}{\ln 2}. \tag{2}$$

The resistance R_1 in the double probe circuit (1–2) was chosen to satisfy the condition $R_1 \ll U_{dc}/I_{is}$ (R_1 was from 5 Ω to 1 kΩ). The resistances R_2 and R_3 were 10 and 30 MΩ.

The triple probe signals passed through a 4-channel opto-coupler (providing high impedance (10^{11} Ω) isolation from ground), and were then recorded in a PC equipped with an analog to digital converter card. Thus the triple probe simultaneously measured I_{is}, T_e and U_{fl}.

The plasma potential (with respect to the grounded anode) was determined from the electron temperature and floating potential measurements [10]:

$$U_{pl} = U_{fl} + \frac{T_e}{e} \ln \sqrt{\frac{\varepsilon M_i}{2\pi m_e}}, \tag{3}$$

where ε is the natural logarithm base and e and m_e are the electron charge and mass, respectively. Plasma density was determined from the I_{is} and T_e using Bohm's expression [10]:

$$I_{is} \approx 0.43 \cdot e n_e \sqrt{\frac{2T_e}{M_i}} S_{pr}, \tag{4}$$

where S_{pr} is the probe collection area and M_i is the ion mass. The ion saturation current density j_{is} was determined as $j_{is} = I_{is}/S_{pr}$.

The probe was movable in the radial direction r, (figure 1) without compromising the vacuum. The probe location (r, z)

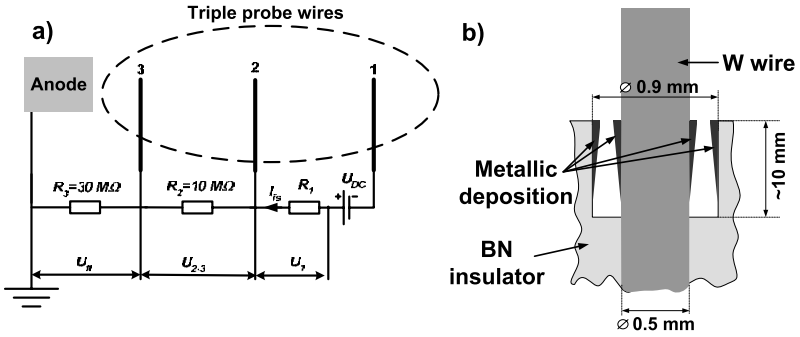

Figure 2. Schematic presentation of triple probe: (*a*) electrical scheme, (*b*) probe wire mounting in the BN insulation with deposition protecting device.

Table 1. Experimental condition for the measurements with the triple probe.

Region	Probe wire arrangement	Collecting area	Anode material	Gap size (mm)	Measured locations
Inside the gap	Probe wires are flush mounted with BN tube	$S_{pr} \approx \frac{\pi D_w^2}{4}$	Graphite	10	$z = 5$ mm; $r = 0$, 8, 16 mm
				6	$z = 3$ mm; $r = 0$, 8, 16 mm
				3	$z = 1.5$ mm; $r = 16$ mm
			Mo	10	$z = 5$ mm; $r = 0$, 8, 16 mm
Outside the gap	Probe wires protruded $l_w = 5$ mm from BN tube	$S_{pr} \approx \pi D_w l_w$	Graphite	10	$z = 5$ mm, $r = 2.5$, 5 cm
			Mo	10	$z = 5$ mm, $r = 5$ cm

was set by radially moving the probe and axially moving the electrode assembly.

Measurements with the triple probe were conducted inside and outside the gap with Mo and graphite anodes. Inside the gap, the graphite anode was used with arc currents $I_{arc} = 175$, 200, 250, 300 and 340 A, while the Mo anode with $I_{arc} = 200$ A. Outside the gap experiments were done in 200 A arc for both electrodes. Note that the probe currents were collected by the end surface of the wires for measurements in the gap and by the lateral surface outside the gap in order to eliminate the contribution of the directed ion velocity [5]. The experimental conditions for measurements with triple probe are summarized in table 1.

The standard method was used to protect the probe from the undesired effects caused by the metallic deposition on it (such as uncontrollable increase in the collecting probe area and the appearance of conductivity between probe wires). It consists of leaving a small gap between the wire and the insulation that prevents the appearance of the continuous film between them [10, 11]. The cross-section of the probe used in this work and equipped with such a protective device is shown in figure 2(*b*). The resistance between the wires was checked before and after each arc experiment and was >200 MΩ (thus for typical voltages between probe wires $\leqslant 10$ V leakage currents were <50 nA). The BN insulation was cleaned from the deposited film after each experiment.

Single probe. Experiments with a single probe were conducted with $I_{arc} = 200$ A and $h = 10$ mm. An assembly with two single probes was used to measure inside the gap. Two single probes were used to obtain plasma parameters at two locations simultaneously in one arc event in order to resolve small changes in plasma parameters in the gap. The two single probes were built into a 6 mm diameter BN tube, each consisting of a W wire with diameter $D_w = 0.5$ mm, separated 3 mm from each other and flush mounted at the end of the BN tube. Thus the current collecting area was $S_{pr} \approx \pi D_w^2/4$. The assembly was oriented such that the two probes were separated in the z-direction. The probe was radially movable and was inserted in the middle of the gap. Measurements with a graphite anode were carried out at $r = 0$, 8, 16 mm. A 50 Hz ac voltage with amplitude 18 V was applied using a transformer, through 2.2 Ω resistors between each probe wire and the grounded anode. Diodes were placed in series in the circuits of each probe to terminate the collection of the large electron current. The applied voltages and signals from the 2.2 Ω resistors were recorded by an oscilloscope. The plasma density, temperature and floating potential were determined at two points ($z = 4$ and 7 mm) from the voltage–current characteristics. The plasma potential was determined, after removing the diodes and measuring the electron saturation current point.

A conventional single probe was used for the measurements outside the gap. In this case the wire protruded $l_w = 5$ mm from the BN tube so that the side of the wire, with an area of $S_{pr} \approx \pi D_w l_w$, collected a major portion of the ion current. The probe was movable in the radial direction, and was positioned at $r = 2.5$, 5, 8, 12, 18 and 19.5 cm at

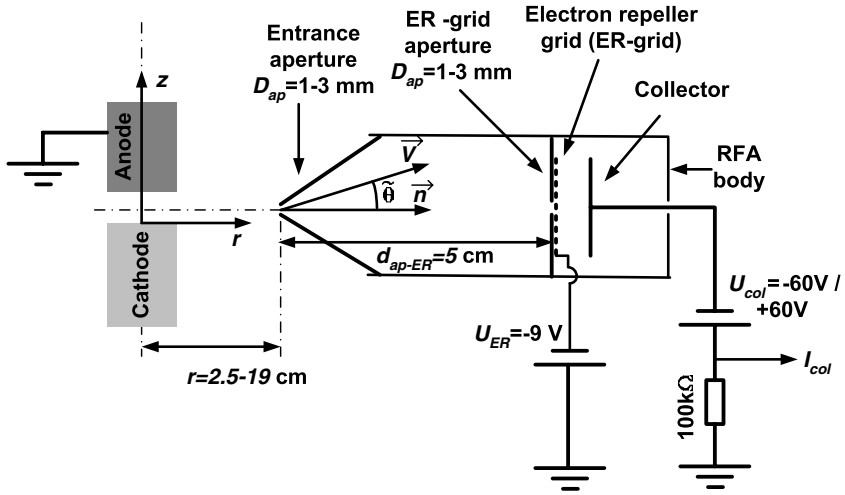

Figure 3. Schematic diagram of the RFA.

the $z = 5$ mm plane, with a graphite anode and at $r = 18$ cm at plane $z = 5$ mm with a Mo anode. AC voltage (50 Hz, 18 V) was applied through resistors (10–10^4 Ω) between the probe wire and the grounded anode. The voltages on the probe and on the shunt were recorded by an oscilloscope and the voltage–current characteristic was determined. The plasma electron temperature T_e was determined from the slope of the voltage–current characteristic in a semi-logarithmic plot, the plasma density was calculated from I_{is}, using equation (4) and U_{pl} was determined graphically [10].

Emissive probe. An emissive probe used two wires which passed through an insulating BN tube, and separated 1 mm from each other (in the z-direction). One of the wires protruded from the BN by ∼5 mm (long wire) such that it had a relatively large collecting area, while the second wire was flush mounted (short wire) and thus had a relatively small area. The voltage–current characteristics of these two single probes were measured as described above for the two single probes.

The probe wires were heated by the plasma during the arc. The long 'hot' wire reached a higher temperature than the short 'cold' one, because the short wire had more efficient 'heat sink' through the wire embedded into BN insulation than the long one, and therefore the long wire thermionically emitted a higher electron current density than the short one. Since the 'hot' and 'cold' wires had different collecting areas, the currents of both wires were normalized to their respective electron saturation currents (at $U = 10$ V). U_{pl} was determined as the voltage at which normalized voltage–current characteristics of the 'hot' and 'cold' probes started to deviate from each other [10, 11]. Measurements were conducted at the $r = 0$, $z = 5$ mm ($I_{arc} = 200$ A, $h = 10$ mm, graphite anode).

RFA design and experimental conditions. Measurements were conducted at the mid-plane of the gap $z = h/2$ for r from 2.5 to 19 cm (see figure 1). The arc currents were $I_{arc} = 200$–350 A, gap distances $h = 5$–20 mm, arc durations up to 120 s and a graphite anode was used.

The ion energy was measured using a RFA, shown in figure 3. The RFA comprised a cylindrical metal body (diameter 44 mm) equipped with a small 25° conical entrance aperture, to reduce the plasma flux. After the entrance aperture, an electron repeller (ER) grid was installed, which repelled all electrons while allowing ions to pass through it. The distance from the cone apex to the ER-grid was $d_{ap–ER} = 50$ mm. The ER grid was covered with a plate having an aperture with diameter D_{ap} from ∼1 to 3 mm, chosen according to the distance from the plasma source, in order to provide sufficiently strong signals. The ER grid was weaved from $D_w = 30\,\mu$m diameter wires with square openings of length $d_h = 50\,\mu$m (grid transmission ∼0.4). A 2 cm diameter collector was installed at a distance $d_{ER\text{-}col} = 2$ mm behind the ER grid. The RFA body and entrance aperture were at floating potential. The ER was at potential −9 V with respect to the grounded anode (since experiments indicate that collector current saturated already at −6 V) and the analyzing collector voltage varied from −60 to +60 V. The collector voltage U_{col} used below in RFA measurements is given with respect to the plasma potential at the RFA entrance. It was determined from directly measured collector voltage with respect to the anode (U_{col}^{an}) as follows: $U_{col} = U_{col}^{an} - U_{pl}$, where U_{pl} is the plasma potential measured as described above. The dependence of the collector current I_{col} versus U_{col} was measured by sweeping U_{col} and approximating the measured I_{col} by continuous exponential functions with polynomial power $-I_{col}(U_{col})$. Then this continuous function $I_{col}(U_{col})$ was differentiated and dI_{col}/dU_{col} was obtained. The ion energy distribution functions and average ion energies were determined via dI_{col}/dU_{col}. Ions extracted from the anode plasma were assumed to be singly ionized [2].

Let us consider the standard approach for analysis of RFA voltage–current characteristics for the cathodic vacuum arc and its modification required for HRAVA. The standard approach establishes the relation between the RFA voltage–current characteristic and the ion distribution function in the vicinity of a cathode spot (VCS), which is a shifted Maxwellian [12–14]. This approach assumes that (1) the distance from the VCS to the RFA entrance is sufficiently large that the

ions may be considered as having been emitted from a point source; (2) the ions arrive at the RFA entrance from the VCS in a solid angle which the RFA entrance subtends from the VCS; (3) the ion energy and momentum weakly vary during their transport from the spot to RFA. The situation is different for measuring close to the gap of a developed HRAVA, since the radial plasma flow originates from a macroscopic plasma source which is of the order of the inter-electrode gap size. Also, the standard approach uses the ion flux distribution function $F^{\mathrm{fl}} = (\mathrm{d}I_{\mathrm{col}}/\mathrm{d}U_{\mathrm{col}})$, which is (citing Kutzner and Miller [13, 15]) 'the cathode ion flux per unit energy in the range E to $E + \mathrm{d}E$ for individual ions of charge number Z_{i} ...'. In this work, the relation between the RFA voltage–current characteristic and the particle distribution function at the RFA entrance ($F^{v}(\vec{V})$) was obtained as described in the appendix. Average ion energies were determined from equation (A6).

The influence of secondary electron emission on the voltage–current characteristic of the RFA used in this work was negligible. It should be noted that the secondary electron current is maximal for high positive U_{col}, since in this case ion current repelled back in the direction of the ER grid is maximal and thus electron emission is also maximal [16]. However, the measurements of the RFA voltage–current characteristic (which will be described below) show that the collector current was zero at high positive U_{col}, thus it may be concluded that the contribution of secondary emission from the ER grid is negligible in the whole examined range of U_{col}.

The measured collector current indicated that the plasma density on the ER grid was $n_{\mathrm{e}} < 2 \times 10^{8}\,\mathrm{cm}^{-3}$. For $|U_{\mathrm{ER\text{-}plasma}}| \sim 9\,\mathrm{V}$, $T_{\mathrm{e}} \sim 1\,\mathrm{eV}$ the electrostatic field penetration depth λ_{p} was about $\lambda_{\mathrm{p}} \approx \lambda_{\mathrm{D}}(eU_{\mathrm{ER\text{-}plasma}}/T_{\mathrm{e}})^{3/4} = 2\,\mathrm{mm}$ [16], which is much more than the grid spacing ($d_{\mathrm{h}} = 50\,\mu\mathrm{m}$) and therefore the ER grid was fine enough to separate plasma components.

The collector current j_{col} did not exceed the current limited by the space charge j_{sp} in the ER-grid-to-collector space (j_{col} was less than $2.5 \times 10^{-5}\,\mathrm{A\,cm}^{-2}$, while for $U_{\mathrm{ER\text{-}plasma}} \sim -9\,\mathrm{V}$, $\langle E_{\mathrm{i}} \rangle \sim 20\,\mathrm{eV}$, $d_{\mathrm{ER\text{-}col}} = 0.2\,\mathrm{cm}$ j_{sp} was $2.7 \times 10^{-5}\,\mathrm{A\,cm}^{-2}$) and thus the space-charge effect may be neglected in this work.

3. Experimental results

3.1. Initial stage and temporal evolution of plasma parameters

Plasma density, electron temperature and plasma potential. Typical temporal evolutions of the electron temperature T_{e}, ion saturation current j_{is} and floating potential U_{fl} obtained from the triple probe are presented in figure 4 for $I_{\mathrm{arc}} = 200\,\mathrm{A}$, $h = 10\,\mathrm{mm}$, $r = 0$, graphite anode. The plasma parameters slightly varied during the initial arc stage ($t < 20\,\mathrm{s}$), while they significantly changed for $t > 20\,\mathrm{s}$ and later at $t > 60\,\mathrm{s}$ they reached steady state (which we will refer to as the 'developed HRAVA stage'). The ion current density and the floating potential increased from $1.5\,\mathrm{A\,cm}^{-2}$ and $-7\,\mathrm{V}$ at the beginning of the arc to $2.0\,\mathrm{A\,cm}^{-2}$ and $-5\,\mathrm{V}$ in the developed HRAVA stage (averaged over 60–90 s), respectively, while the electron temperature was maximal at the beginning of the arc (~2.3 eV)

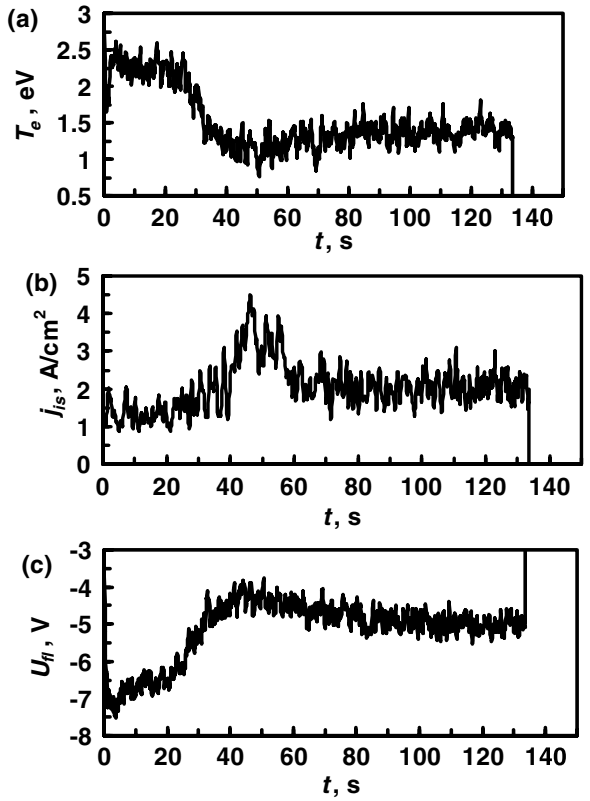

Figure 4. Plasma parameter evolutions measured by the triple probe for $h = 10\,\mathrm{mm}$, $I_{\mathrm{arc}} = 200\,\mathrm{A}$, $r = 0$, graphite anode.

and then decreased to 1.4 eV during the developed HRAVA stage. A local maximum of j_{is}, exceeding $4\,\mathrm{A\,cm}^{-2}$, was observed at $t \sim 40$–$50\,\mathrm{s}$, and there was also a local maximum in U_{fl} and a minimum in T_{e} at approximately the same time. The anode plasma plume was visually observed starting from $t \sim 20\,\mathrm{s}$, while the cathode material was completely removed from the anode after $t \sim 60\,\mathrm{s}$ (for $I_{\mathrm{arc}} = 200\,\mathrm{A}$). Plasma potential (determined using equation (3)) was about 5.5 V in the initial arc stage ($t < 20\,\mathrm{s}$) and then decreased to 2.4 V at steady state ($t > 60\,\mathrm{s}$) for $I_{\mathrm{arc}} = 200\,\mathrm{A}$, $h = 10\,\mathrm{mm}$, $r = 0$. Note that the potential drop in the anode sheath is close to the above mentioned plasma potential, since the probe was located close to the anode and U_{pl} is measured with respect to the anode.

Plasma parameter measurement error was governed by signal fluctuations and did not exceed 10% in the developed HRAVA stage and 20% in the initial stage. Plasma parameters were not dependent on the anode material within the measurement error (graphite and Mo anodes were tested). Plasma parameters measured with the triple and single probes under the same experimental conditions ($h = 10\,\mathrm{mm}$, $I_{\mathrm{arc}} = 200\,\mathrm{A}$, $r = 2.5$ and 5 cm) agreed within 10%.

Ion energy. Typical smoothed RFA voltage–current characteristics are given in figure 5 for two distances from the electrode axis, $r = 2.5$ and 19 cm ($t \sim 5\,\mathrm{s}$ after arc ignition, $h = 10\,\mathrm{mm}$, $I_{\mathrm{arc}} = 200\,\mathrm{A}$). The additional curve presented in figure 5 was obtained under similar conditions for $t = 20\,\mathrm{s}$, $r = 19.6\,\mathrm{cm}$, $I_{\mathrm{arc}} = 175\,\mathrm{A}$ previously by Beilis *et al* [4, 5]. It is seen that the RFA voltage–current characteristics are

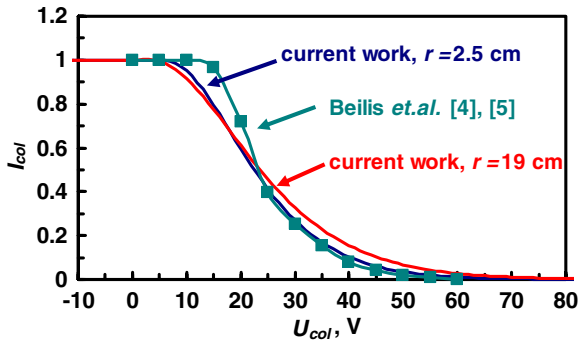

Figure 5. RFA voltage–current characteristics measured in this work (for $I_{arc} = 200$ A, $r = 2.5$ and 19 cm, $h = 10$ mm, $t \sim 5$ s after arc ignition) and reported previously by Beilis *et al* [4, 5] in similar conditions. The I_{col} values are normalized to their saturation value.

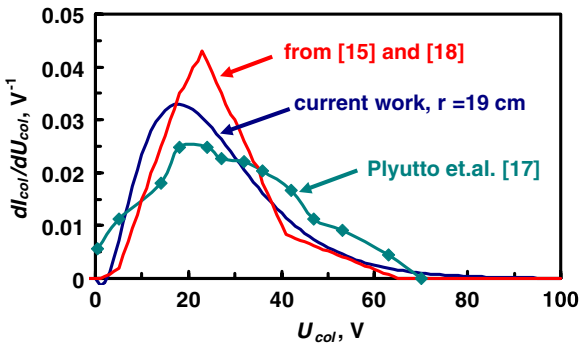

Figure 6. The dependences of dI_{col}/dU_{col} obtained in this work (for $I_{arc} = 200$ A, $r = 1.6$ and 19 cm, $h = 10$ mm, $t \sim 5$ s after arc ignition) and comparison with previous data [15, 17, 18].

in fair agreement. The dependences of dI_{col}/dU_{col} on U_{col} obtained in this work are shown in figure 6 (dimensionless and normalized to unit I_{col} was used). Two additional curves, for Cu vacuum arcs, are presented for comparison. The first one was previously reported for a 100 A arc by Plyutto *et al* [17]. The second was obtained from the data for peak voltages of singly, doubly and triply charged ions presented by Davis and Miller [18] for radially expanded flux, using a triangle approximation for the ion flux distribution function and data for half-widths of $F_{fl}(E_i)$ published later by Kutzner and Miller [15]. It is seen that dI_{col}/dU_{col} are in fair agreement with previous data published in the literature.

The evolution of the voltage–current characteristic with arcing time is presented in figure 7 ($I_{arc} = 250$ A, $r = 19$ cm, $h = 5$ mm). It is seen that with transition from the initial stage to the developed HRAVA stage the whole voltage–current characteristic moved to the lower U_{col} values. This results in shifting of the dI_{col}/dU_{col} maximum to lower collector voltages as shown in figure 8 for the same conditions.

3.2. Developed stage

Inter-electrode plasma parameters. Throughout this section, the time averaged values of the plasma parameters in the developed HRAVA stage (60–90 s from arc ignition) will be presented. The dependence of the n_e at $r = 0$ and at the anode radius $r = R_a$ on I_{arc} for $h = 10$ mm is presented in figure 9.

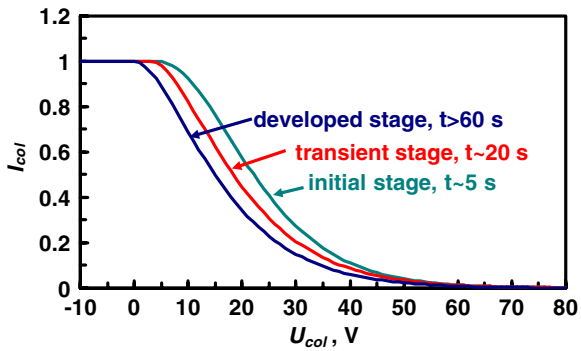

Figure 7. Evolution of the RFA voltage–current characteristic with transition to the developed HRAVA stage ($I_{arc} = 250$ A, $r = 19$ cm, $h = 5$ mm). I_{col} is normalized to its saturation value.

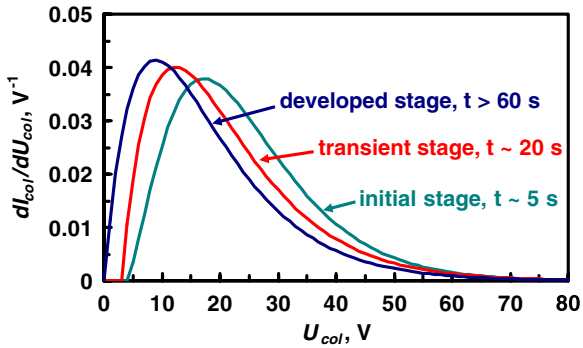

Figure 8. Evolution of dI_{col}/dU_{col} with transition to the developed HRAVA stage ($I_{arc} = 250$ A, $r = 19$ cm, $h = 5$ mm, dimensionless and normalized to unit I_{col} is used).

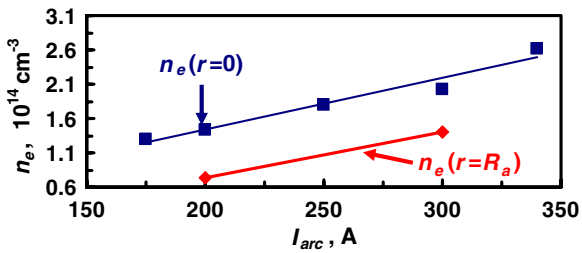

Figure 9. Plasma density at the gap mid-plane in the developed HRAVA versus arc current (measured with the triple probe, $r = 0$, $h = 10$ mm).

It was observed that the plasma density increased linearly with the arc current. The dependence of T_e versus I_{arc} for $h = 6$ and 10 mm is presented in figure 10. It is seen that T_e increased with I_{arc} and decreased slightly with h.

Typical radial distributions of the inter-electrode plasma parameters are presented in figure 11 for $h = 3$, 6 and 10 mm. It was observed that (1) T_e, n_e and U_{pl} decreased with r, (2) T_e, n_e and U_{pl} decreased with h, (3) T_e became more uniform with smaller gaps, (4) U_{pl} decreased by $\sim$1 V from the axis to $r = R_a$ and (5) the ratio $n_e(r = 0)/n_e(r = R_a)$ slightly decreased with I_{arc} (from 1.9 to 1.45 for $I_{arc} = 200$ and 300 A, respectively, $h = 10$ mm) and increased with h (from 1.55 to 1.9 for $h = 6$ and 10 mm respectively, $I_{arc} = 200$ A).

The longitudinal distribution of plasma parameters was measured using the assembly with two single probes. Typical

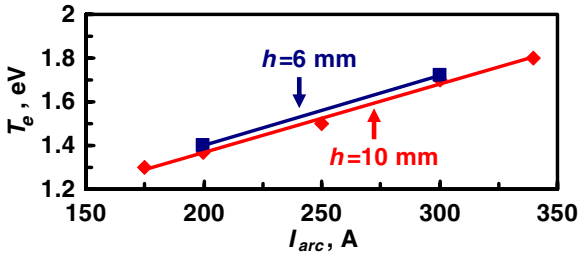

Figure 10. T_e at the gap mid-plane in the developed HRAVA versus arc current (measured by triple probe, $r = 0$, $h = 6$ and 10 mm).

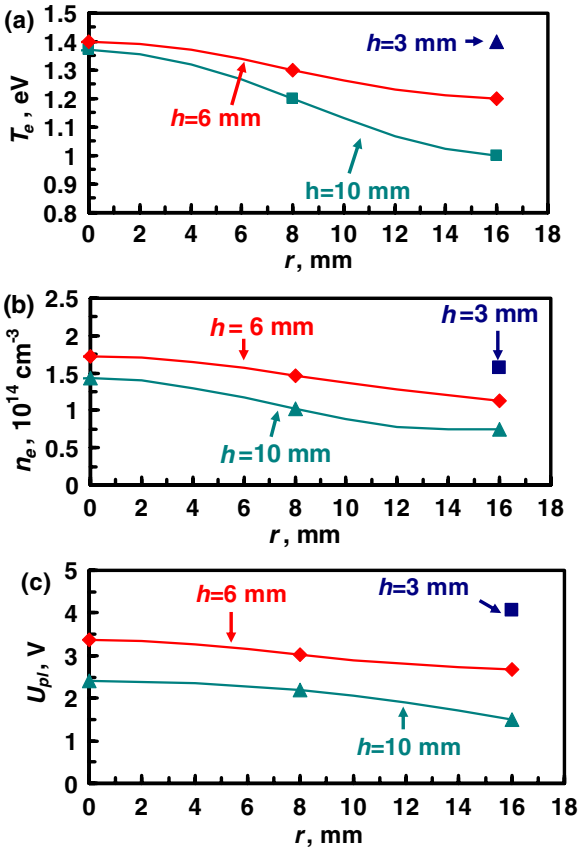

Figure 11. Radial distribution of plasma parameters in the gap mid-plane in the developed HRAVA ($h = 3$, 6, 10 mm, $I_{arc} = 200$ A, triple probe).

ion current portions of the voltage–current characteristics obtained with $I_{arc} = 200$ A, $r = 0$ and $h = 10$ mm are shown in figure 12 with (*a*) linear and (*b*) semi-logarithmic scales. At both measured points ($z = 4$ and 7 mm), it was found that $T_e \sim 1.4$ eV, $n_e \sim 1.4 \times 10^{14}$ cm^{-3}, $U_{fl} \sim -5$ V (within experimental error, caused by signal fluctuations of ± 0.25 eV, $\pm 0.2 \times 10^{14}$ cm^{-3} and ± 0.2 V, respectively). The plasma potentials U_{pl} determined by single probe and U_{pl} determined by triple probe (from U_{fl} and T_e according to equation (3)) were close (e.g. 2.6 V and 2.4 V, respectively, for $I_{arc} = 200$ A, $r = 0$ and $h = 10$ mm; see figure 11).

The plasma potentials can also be directly obtained from the electron current part of the voltage–current characteristic $j(U)$ shown in figure 13. The point where the electron current saturated is clearly seen. It may also be seen that the plasma

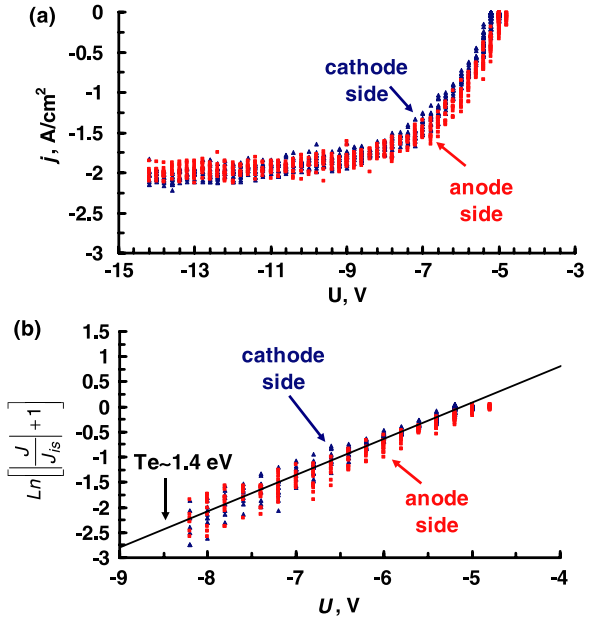

Figure 12. Voltage–current characteristic in the developed HRAVA on (*a*) linear and (*b*) semi-logarithmic scales for $I_{arc} = 200$ A, $r = 0$, $h = 10$ mm. Triangles: cathode side, $z = 4$ mm; squares: anode side, $z = 7$ mm.

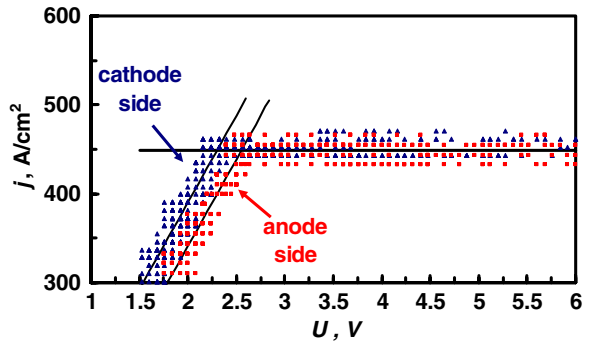

Figure 13. Electron port of the voltage–current characteristic in the developed HRAVA for $I_{arc} = 200$ A, $r = 0$, $h = 10$ mm (Triangles: cathode side, $z = 4$ mm; squares: anode side, $z = 7$ mm).

potential increased slightly from 2.3 V near to the cathode to 2.6 V near to the anode.

The smoothed two-dimension (2D) distribution of the plasma potential in a 10 mm gap and for 200 A arc is presented in figure 14 (graphite anode). It is seen that U_{pl} increased from the cathode to the anode and decreased with r. It should be noted that in the U_{pl} measurements shown in figures 13 and 14 using the assembly with two single probes, the probe wires were heated by the large electron current, which increased the apparent floating potential and the apparent absolute value of the ion saturation current, due to electron emission from the probe wires [11]. To prevent this in cases where the electron current was saturated, the probe was inserted into the gap only for only a few seconds to minimize wire heating.

In addition, U_{pl} was measured by the emissive probe at the gap center ($I_{arc} = 200$ A, $h = 10$ mm). It was observed that the large area probe was brightly luminescent, indicating that it was significantly heated. Its voltage–current

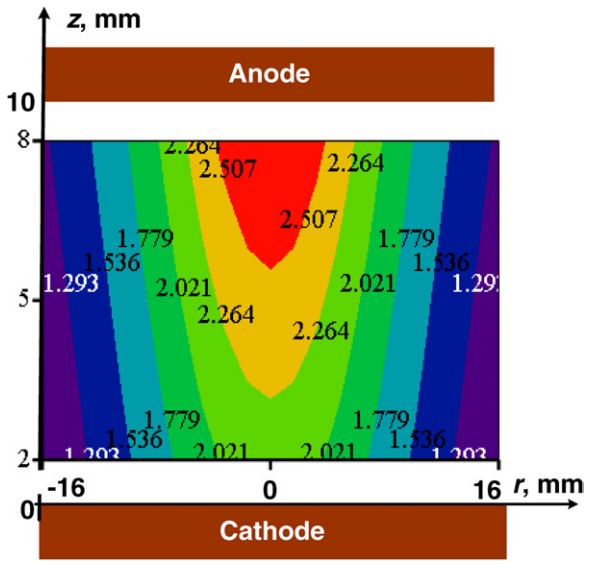

Figure 14. 2D distribution of the plasma potential in a 10 mm gap for $I_{arc} = 200$ A (developed HRAVA stage, graphite anode).

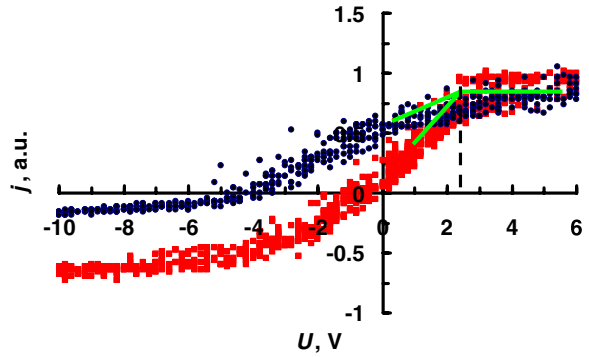

Figure 15. Voltage–current characteristic of the emissive probe. Squares—large area hot probe; circles—small area probe. Deviation of two voltage-current characteristics is indicated by the lines.

characteristic is presented in figure 15 (squares). The voltage–current characteristic of a small area probe is indicated by circles in figure 15. From the comparison of these, it is seen that the absolute value of the saturated current density at negative voltages was higher and U_{fl} was more positive with the large area probe. The voltage–current characteristics coincided starting for $U_{pl} > 2.4$ V (the same value of U_{pl} was measured with the assembly of 2-single probes, see figure 13).

Plasma parameters outside the gap. The radial distributions of the developed HRAVA stage plasma parameters are presented in figure 16 for $I_{arc} = 200$ A, $h = 10$ mm, $z = 5$ mm. It is seen that n_e, T_e and U_{pl} decreased with r. T_e and U_{pl} decreased rapidly with r (1.6 cm $< r <$ 5 cm) and slower at $r > 5$ cm. Outside the gap n_e decreased approximately as $1/r^2$.

The steady-state voltage–current characteristics of the RFA (for the developed HRAVA stage) at $r = 2.5$, 10 and 19 cm are shown in figure 17 ($I_{arc} = 200$ A, $h = 10$ mm). It is seen that the falling part of the characteristic shifted to higher collector voltages with increasing r, indicating higher ion energies.

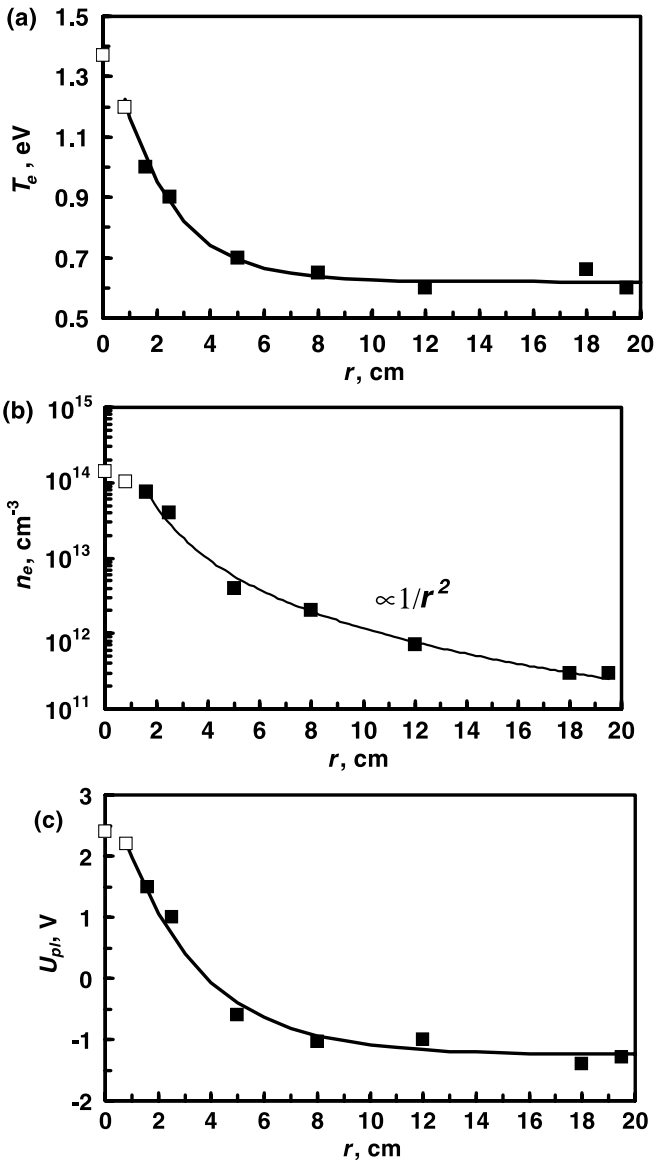

Figure 16. Radial distribution of plasma parameter in the developed HRAVA ($I_{arc} = 200$ A, $h = 10$ mm, $z = 5$ mm). Open symbols indicate plasma parameters inside the gap.

The dependence of the average energy of ions $\langle E_i \rangle$ (calculated according to (A6)) moving in the radial direction (with $(V_z/V_r) \ll 1$, where V_z and V_r are the axial and radial components of ion velocity, respectively, see the appendix) versus r is presented in figure 18 for $I_{arc} = 200$ A, $h = 10$ mm. It is seen that $\langle E_i \rangle$ increases from ~8 eV at $r = 2.5$ cm to the ~14 eV at $r = 19$ cm. At $r = 2.5$ cm $\langle E_i \rangle$ was ~8–9 eV for $h = 5$, 10 mm and $I_{arc} = 200$ and 300 A.

The dependences of $\langle E_i \rangle$ on arc current and gap size are presented in figures 19 and 20, respectively. It was observed that $\langle E_i \rangle$ was in the range 14–15 eV and only slightly decreased with I_{arc} and h.

4. Discussion

The above experiments demonstrated the temporal evolution of the plasma parameters from arc initiation till the steady state

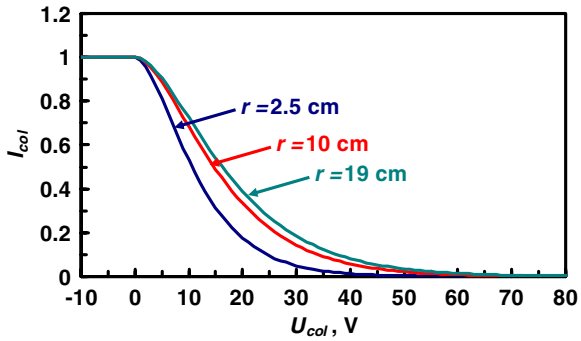

Figure 17. Voltage–current characteristics of the RFA at $r = 2.5$, 10 and 19 cm ($I_{arc} = 200$ A, $h = 10$ mm). The I_{col} values are normalized to their saturation value.

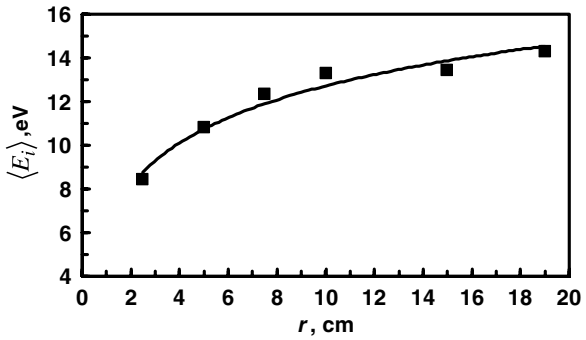

Figure 18. Dependence of $\langle E_i \rangle$ versus r for $I_{arc} = 200$ A, $h = 10$ mm.

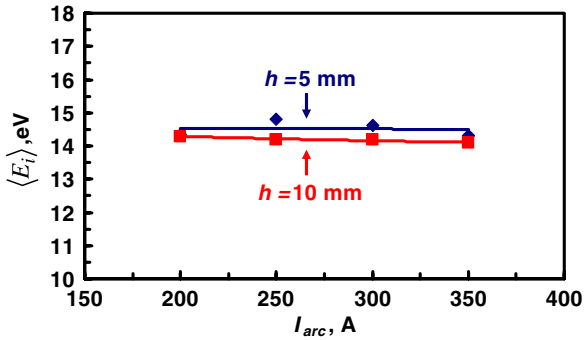

Figure 19. Dependence of $\langle E_i \rangle$ on I_{arc} for $r = 19$ cm, $h = 5$ and 10 mm.

was reached. The current setup presents a unique opportunity for studying two arc modes: (i) the conventional cathodic arc in the initial stage (ii) and the developed HRAVA when all cathode material was re-evaporated from the hot anode and the anode no longer collects cathode material. Let us discuss the measured evolution of plasma parameters in HRAVA.

Evolution of plasma parameters in HRAVA. After arc initiation, while the anode is relatively cold, it passively collects material emitted from the cathode spots. During this time ($t < 20$ s for $I_{arc} = 200$ A), the arc operates as a conventional cathodic arc. Thus the plasma parameters during this initial stage were close to those previously measured for cathodic vacuum arcs. The electron temperature measured during the initial stage was ~2.3 eV for 200 A, which is close

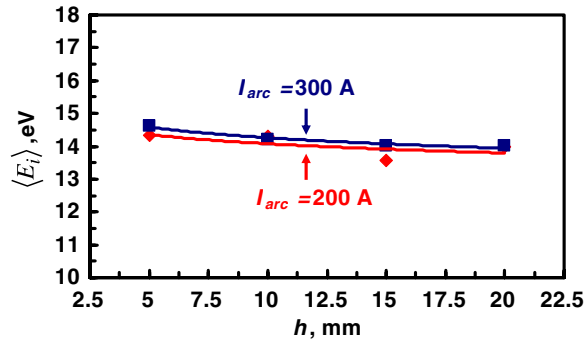

Figure 20. Dependence of $\langle E_i \rangle$ on gap size ($r = 19$ cm, $I_{arc} = 200$ and 300 A).

to that found by Kutzner and Glinkowski [19] −2.0–3.2 eV and Rakhovsky [20] −2.0–2.6 eV for Cu arcs with $I_{arc} \approx$ few hundred amperes. Ion flux distribution functions found in the initial stage in this work were close to those previously found by Plyutto *et al* [17] and Davis and Miller [18] (see figure 6).

As the anode is heated by the arc with time the additional Cu atom flux is supplied to the gap [2]. Let us consider the mechanisms responsible for this Cu flux. At first, the material eroded (including MPs) from the cathode reaches the anode surface, and condenses thereon. At a sufficiently high temperature, this material is re-evaporated supplying additional Cu atoms to the gap. Another mechanism of Cu atoms production is that MPs are heated in the inter-electrode plasma and may be evaporated during their flight through the gap [3]. These additional Cu atoms produced in the gap at HRAVA development are ionized in the oncoming plasma jets [2] and cause the increase in plasma density observed experimentally (see figure 4).

Now let us consider ion energy and electron temperature temporal evolution, related to the development of the anode plasma plume. According to theoretical predictions, the cathodic plasma jets are dissipated in anode plasma [2]. As a result, the high energy ions and electron temperature decrease from the value in the cathode jet to lower these parameters in the anode plasma. This coincides with a measured shift of the ion flux energy distribution to lower energies (the maximum shifts from $U_{col} \sim 20$ V at $t \sim 5$ s to $U_{col} \sim 10$ V at $t > 60$ s; see figure 8) and a decrease in the electron temperature (from ~2.3 eV to ~1.4 eV in the gap center).

HRAVA characteristic times. After arc initiation, the anode surface is heated by the arc and the cathode plasma jets deposit cathode material upon it. When the anode is sufficiently hot, the atoms re-evaporated from the hot anode form a vapor cloud near the anode; these atoms are impacted and ionized by the oncoming cathode jets [2]. This changes the plasma parameters and forms a visible luminous anode plasma plume at $t \approx 20$ s, which signifies the end of the initial stage ($t < 20$ s) and the beginning of a transient stage. The transient stage is characterized by anode plasma plume development, and is finished at $t \sim 60$ s when the cathode material is completely removed from the anode surface and the plasma parameters reach steady state. It should be noted that n_e had a maximum at $t_{max} \sim 40$–50 s during the transient stage where it exceeded

its steady-state value. This maximum may be explained by the re-evaporation of the Cu atoms which accumulated on the anode surface during the whole initial stage. During the transient stage this accumulated material is removed. In the steady state the re-evaporated flux is equal to the incoming flux, while in the transient stage there is no such limitation and the re-evaporated flux was higher than the incoming flux near the maximum due to re-evaporation of the accumulated cathode material. It should further be noted that T_e had a minimum at $t = 50$ s, i.e. when n_e was maximal. Possibly this may also be attributed to the maximum in the 'cold' atom flux from re-evaporation from the anode, which would tend to cool the plasma.

The discharge was in the developed HRAVA stage for $t > 60$ s (for $I_{arc} \sim 175$–200 A). It was previously shown that the anode temperature continued increasing for $t > 60$ s and reached steady state at 100–110 s for graphite anodes [21] and 130–140 s for Mo anodes [22]. Achieving steady-state plasma parameters while the anode temperature continued to increase may be explained by noting that once the anode was already sufficiently hot to re-evaporate all of the incoming cathode material, further increase in the anode temperature has little, if any, effect on the plasma parameters. The steady-state anode temperature is determined by the anode energy balance, and depends on thermophysical properties of the anode material.

Developed HRAVA stage: plasma density and electron temperature. A uniform distribution of n_e and T_e along z was observed experimentally in the HRAVA with a gap of $\leqslant 10$ mm (see figure 12), which agrees with the theoretical model of the HRAVA [2]. Thus n_e and T_e in the developed HRAVA gap may be considered as functions of single spatial variable r (for symmetric anodes).

Let us consider the steady-state radial distributions of n_e and T_e. The observed increase in n_e in the gap during the transition to the developed HRAVA (due to ionization of Cu vapor in the gap) is limited by the radial plasma outflow, which increases as plasma density increases in the gap. Finally a steady-state plasma density distribution is established when the cathode mass loss rate is equal to the area integral of the radially expanded mass flux (since in the developed HRAVA stage there is no condensation on the hot anode). According to the theoretical model [2], the ratio $(n_e(r = 0)/n_e(r = R_a)) = \exp(0.5) \approx 1.65$ should be established, which is close to that found experimentally ($\sim$1.45–1.9) (see figure 11). The predicted average plasma densities were 1.5×10^{14} cm^{-3} and 2.8×10^{14} cm^{-3} for $I_{arc} = 175$ A and 340 A, respectively [2]. The experimental values, averaged over the gap, were lower by about 1.5 times and this may be explained by a lower ionization degree than the 100% used in the theory [23]. The plasma electron temperature, predicted by Beilis *et al* [2] from the energy balance, decreased with time, reaching $\sim$1 eV in the developed HRAVA stage; this is supported by the measurements (see figure 4). The radial distribution of T_e became more uniform in smaller gaps (see figure 11) supporting the assumption previously used [2]. The linear increase in plasma density in the gap with the arc current (figure 9) is caused by the proportional increase in the mass emission into the gap from the cathode.

Outside the gap, the measured plasma density distribution is approximated well by a $1/r^2$ dependence (figure 16(*b*)). This agrees with the predictions of an MHD model [8] of significant deviation from the pure radial expansion with constant velocity ($\sim 1/r$) due to the axial plasma expansion and ion acceleration in the plasma pressure gradient (considered later).

Let us consider the resistivity of the anode plasma plume filling the gap. In the developed HRAVA, when cathodic plasma jets are dissipated in the dense anode plasma plume, arc current is conducted through the whole inter-electrode gap. Plasma resistivity may be estimated from

$$\rho_{pl} = 5.2 \times 10^{-3} \frac{\ln \Lambda}{T_e^{3/2}(\text{eV})}\ \Omega\,\text{cm},$$

where $\ln \Lambda$ is the Coulomb logarithm [24]. Using the plasma parameters measured in the 200 A arc with a 10 mm gap ($n_e = 10^{14}$ cm^{-3}, $T_e = 1.2$ eV), the resistance of the plasma gap was calculated to be $\sim 5 \times 10^{-3}\ \Omega$ and thus the potential drop (for $I_{arc} = 200$ A) in the plasma column was $\sim$1 V. This agrees well with the directly measured plasma potential (figure 14).

Plasma parameters measured in the developed HRAVA, both inside and outside the gap, depended only slightly on the anode material. This may be because once the anode which reached a temperature sufficient for evaporating all cathode material impinging on it, it may be modeled as an 'ideal reflector' of the entire incoming mass flux, and differences in the considered anode material constants are no longer relevant.

Developed HRAVA stage: ion acceleration. Measured ion acceleration in the radial direction may be explained by a plasma pressure gradient [2, 8]. The ion energy growth ΔE_i during radial plasma expansion from $r = r_1$ to $r = r_2$ may be expressed (for constant temperature T_e) as:

$$\Delta E_i = T_e \ln \frac{n_e(r_1)}{n_e(r_2)}, \tag{5}$$

where $n_e(r_1) > n_e(r_2)$. Two cases will be considered: (1) expansion of plasma limited by the arc electrodes and (2) plasma expansion with a free boundary outside the gap.

The slight dependence of the ion energy at $r = 2.5$ cm on the arc current and gap size ($\sim$8–9 eV for $I_{arc} = 200$, 300 A and $h = 5$, 10 mm) may be explained by a small change in the ratio $n_e(r = 0)/n_e(r = R_a)$ inside the gap for different I_{arc} and h. Indeed the ratio $n_e(r = 0)/n_e(r = R_a)$ was measured to be $\sim$1.45–1.9 for $I_{arc} = 200$, 300 A and $h < 10$ mm, while T_e changed slightly. Thus, according to equation (5), the accelerated ions energy varied slightly at $r = 2.5$ cm for different arc currents and gap sizes.

Now let us consider measured ion acceleration outside the gap (figure 18). The radial plasma density decreased outside the gap (from $n(r_1 = 1.6\,\text{cm}) = 8 \times 10^{13}$ cm^{-3} to $n(r_2 = 19\,\text{cm}) = 3 \times 10^{11}$ cm^{-3} for $I_{arc} = 200$ A); this provided a gradient of the plasma pressure. Thus according to equation (5) and for $T_e = 1$ eV, the ions should gain an energy of $\sim$5.6 eV which is close to the measured value $\sim$5 eV. The only slight dependence of ion energy on I_{arc} and h may indicate

Table 2. Comparison of measured ($h = 10$ mm, $r = 0$) and theoretically predicted [2]) plasma parameters in the developed HRAVA inside the inter-electrode gap.

	$I_{arc} = 175$ A		$I_{arc} = 340$ A	
	Experiment	Theory [2]	Experiment	Theory [2]
n_e (cm^{-3})	1.3×10^{14}	1.5×10^{14}	2.6×10^{14}	2.8×10^{14}
U_{arc} (V)	20.4	23.3	22.5	24.2
U_a (V)	2.4[a]	2.4	3.4[b]	2.9
T_e (eV)	1.3	0.9	1.8	1

[a] $I_{arc} = 200$ A.
[b] $I_{arc} = 300$ A.

that T_e and the ratios $(n_e(r = 1.6\,\text{cm}))/(n_e(r = 19\,\text{cm}))$ were close for different I_{arc} and h.

Total electron current to the anode may be determined as $I_e = \int_{S_a} j_e \mathrm{d}S$, where $j_e \cong j_{th} \exp(-(|eU_a|/T))$ is the electron current density at the anode surface, $j_{th} = \frac{1}{4} e n_e V_{T_e}$ is the thermal electron current at the anode sheath entrance and U_a is the anode potential drop that is equal to the plasma potential near the anode. Using measured n_e, T_e and U_{pl} near the anode, it was found that I_e and I_{arc} were close (deviations between them were within 10% of I_{arc}). Plasma parameters in the developed HRAVA inside the inter-electrode gap measured in this work ($h = 10$ mm, $r = 0$) and predicted theoretically by Beilis *et al* in [2] are summarized in table 2.

5. Conclusions

(1) In the initial stage of the arc (i.e. the first 20 s of arcing for $I_{arc} \sim 200$ A), when anode was relatively cold, the arc operated in the conventional cathodic arc mode. The electron temperature and ion energy distribution were close to that previously measured in conventional cathodic vacuum arcs.
(2) Plasma density in the gap increased with HRAVA development. The plasma density reached the steady state (1 min after arc ignition for $I_{arc} \sim 200$ A), signifying the beginning of the developed HRAVA stage and confirming the result predicted in [7] that cathode erosion is balanced by the radial plasma outflow. In the developed HRAVA, the gap was filled by a dense anode plasma plume with plasma density $n_e > 10^{14}$ cm^{-3} which was uniform in the axial direction and decreased radially with $(n_e(r = 0)/n_e(r = R_a)) = 1.45$–$1.9$ (for $I_{arc} = 200$ and 300 A, $h = 6$ and 10 mm) that is in accordance with theory [2].
(3) Relatively slow ions at the gap exit in the developed HRAVA were accelerated as the plasma expanded from the HRAVA gap in the gradient of plasma pressure. The ion energy was ~15 eV at 19 cm from the electrodes, and it weakly depended on the arc current and gap size.
(4) The measured plasma density, electron temperature, ion energy, anode heat flux and temperature agreed with a previously formulated theory [2].

Acknowledgments

This research was supported by a grant from the Israel Science Foundation. The authors thank Mr Dmitry Grach for the opto-coupler construction. In addition, the authors gratefully acknowledge the technical assistance of Mr Michael Govberg and Mr Jakob Zalcman.

Appendix

Let us determine the relation between ion velocity distribution function and RFA voltage–current characteristic applicable for any width of ion distribution function in velocity space which was not previously considered. This result will be applied for the case of narrow distribution function (see below) in order to obtain the average energy of ions $\langle E_i \rangle$ from the RFA voltage–current characteristic and the dependence of $\langle E_i \rangle$ on discharge parameters (distance to electrodes, arc current). We will consider singly charged ions with an ion velocity distribution function $F^v(\vec{V})$ at the analyzer entrance (at the cone apex in figure 3), normalized to unit density $\int_{-\infty}^{\infty} F^v(\vec{V}) \mathrm{d}^3\vec{V} = 1$, i.e. $F^v(\vec{V})\mathrm{d}^3\vec{V}$ is the fraction of ions having velocities in a differential volume of velocity space $\mathrm{d}^3\vec{V}$ adjacent to $\vec{V}$. Assuming uniformity of the plasma parameters across the entrance aperture, the total current entering the analyzer may be written:

$$I = j_n S_{ap} \propto \int_{V_\parallel > 0} F^v(\vec{V}) V_\parallel \mathrm{d}^3\vec{V},$$

where $S_{ap} = (\pi D_{ap}^2/4)$ is the aperture area, $V_\parallel$ is the component of the ion velocity along $\vec{n}$ (figure 3) and j_n is the normal component of the ion current density at the aperture position. If U_{col} is the collector potential with respect to the plasma potential at the analyzer entrance, and if the RFA diameter is large enough so that losses of the ions on the RFA walls during their flight from the entrance aperture to the collector are negligible, the collector current may be written as

$$I_{col}(U_{col}) \propto \int_{V_\parallel > \sqrt{2eU_{col}/M_i}} F^v(\vec{V}) V_n \mathrm{d}^3\vec{V}$$

$$= \int_{V_\parallel > \sqrt{2eU_{col}/M_i}} F^v(V, \tilde{\theta}, \tilde{\varphi}) V_\parallel V^2 \sin\tilde{\theta}\, \mathrm{d}V\, \mathrm{d}\tilde{\theta}\, \mathrm{d}\tilde{\varphi}, \quad \text{(A1)}$$

where V is the absolute value of the particle velocity, $(V, \tilde{\theta}, \tilde{\varphi})$ is a spherical coordinate system in velocity space, where $\tilde{\theta}$ is computed from the $\vec{n}$ (figure 3). Weak variation of the ion energy and momentum during their transport from the RFA entrance to the ER grid is assumed. Assumptions concerning the distribution function are required for the following analysis. Let us assume that the ion distribution function is isotropic

within a cone with angle $2\tilde{\theta}^*$ and zero outside it. In this case $F^v(V, \tilde{\theta}, \tilde{\varphi})$ can be expressed as

$$F^v(V, \tilde{\theta}, \tilde{\varphi}) = F^v(V)\Theta(\tilde{\theta} - \tilde{\theta}^*), \tag{A2}$$

where

$$\Theta(\tilde{\theta} - \tilde{\theta}^*) = \begin{cases} 1, \tilde{\theta} < \tilde{\theta}^* \\ 0, \tilde{\theta} > \tilde{\theta}^* \end{cases}.$$

Substituting the ion velocity distribution function $F^v(V, \tilde{\theta}, \tilde{\varphi})$ in the form given by equation (A2), using that $V_\parallel = V\cos\tilde{\theta}$ and integrating along angle $\tilde{\varphi}$, an expression for the collector current, equation (A1) may be re-written as

$$I_{\mathrm{col}}(U_{\mathrm{col}}) \propto \int_0^{\tilde{\theta}^*} \int_{\frac{1}{\cos\tilde{\theta}}\sqrt{\frac{2|e|U_{\mathrm{col}}}{M_i}}}^{\infty} F^v(V) V^3 \sin\tilde{\theta}\cos\tilde{\theta}\,\mathrm{d}V\,\mathrm{d}\tilde{\theta}.$$

After the calculation of the first derivative of the current with respect to U_{col} and using the ion velocity distribution function expressed in terms of energy, it may be obtained that

$$\frac{\mathrm{d}I_{\mathrm{col}}}{\mathrm{d}U_{\mathrm{col}}} \propto -\int_{|e|U_{\mathrm{col}}}^{|e|U_{\mathrm{col}}/\cos^2(\tilde{\theta}^*)} F^v(E)\,\mathrm{d}E. \tag{A3}$$

Equation (A3) is applicable for the case of arbitrary angle $\tilde{\theta}^*$. Let us consider two different cases.

For $\tilde{\theta}^* = \pi/2$, i.e. for an isotropic ion distribution function at the analyzer entrance:

$$\frac{\mathrm{d}I_{\mathrm{col}}}{\mathrm{d}U_{\mathrm{col}}} \propto -\int_{|e|U_{\mathrm{col}}}^{\infty} F^v(E)\mathrm{d}E \Rightarrow \frac{\mathrm{d}^2 I_{\mathrm{col}}}{\mathrm{d}U_{\mathrm{col}}^2} \propto F^v(|e|U_{\mathrm{col}}). \tag{A4}$$

This relation is the same as the well-known expression for electron current to a flat probe for an isotropic electron distribution function [11].

In the other extreme case, for small $\tilde{\theta}^* \ll 1$ it may be obtained that

$$\frac{\mathrm{d}I_{\mathrm{col}}}{\mathrm{d}U_{\mathrm{col}}} \propto -F^v(|e|U_{\mathrm{col}})U_{\mathrm{col}}. \tag{A5}$$

This relation coincides with the expression obtained by Beilis *et al* [5].

It should be noted that applying (A4) ($\tilde{\theta}^* = \pi/2$) for an isotropic ion distribution at the RFA entrance is problematic in the real situation, because only ions having velocity vectors lying inside the solid angle from which the collector is seen from the entrance aperture contribute to the collector current, while ions entering the RFA at larger angles hit the RFA walls. This means that ion collector current will be collected only partially and there will be deviations from (A4).

The RFA used in this work was equipped with two apertures (at the entrance and aperture on the ER grid) with $D_{\mathrm{ap}} \leqslant 3$ mm placed at a distance $d_{\mathrm{ap-ER}} = 50$ mm from the entrance, and thus only ions with velocity vectors at the entrance aperture almost parallel to $\vec{n}$ contributed to the collector current:

$$\frac{V_\perp}{V_\parallel} \leqslant \tilde{\theta}_{\mathrm{RFA}} \approx \frac{D_{\mathrm{ap}}}{d_{\mathrm{ap-ER}}} \ll 1,$$

where $V_\perp$ and $V_\parallel$ are the components of velocity perpendicular and parallel to $\vec{n}$. The value of $\tilde{\theta}_{\mathrm{RFA}}$ was chosen (by choosing of the aperture diameters) to be smaller than the angular width of the ion distribution function in velocity space, $\tilde{\theta}_{\max}$ [23] and the ion distribution function was assumed to be isotropic inside $\tilde{\theta} \leqslant \tilde{\theta}_{\mathrm{RFA}}$. Therefore (A3) is applicable with $\tilde{\theta}^* = \tilde{\theta}_{\mathrm{RFA}}$, and finally, due to the smallness of $\tilde{\theta}_{\mathrm{RFA}}$, the ion distribution function should be determined from (A5). An average energy of ions moving in directions close to $\vec{n}$ may be expressed from the voltage–current characteristic and using (A5) as

$$\langle E_i \rangle = \frac{\int_0^\infty F^v(\vec{V})\dfrac{MV^2}{2}\,\mathrm{d}^3\vec{V}}{\int_0^\infty F^v(\vec{V})\,\mathrm{d}^3\vec{V}} = \frac{\int_0^\infty F^v(E)E^{3/2}\,\mathrm{d}E}{\int_0^\infty F^v(E)E^{1/2}\,\mathrm{d}E}$$

$$= |e|\frac{\int_0^\infty \sqrt{U_{\mathrm{col}}}\dfrac{\mathrm{d}I_{\mathrm{col}}}{\mathrm{d}U_{\mathrm{col}}}\,\mathrm{d}U_{\mathrm{col}}}{\int_0^\infty \dfrac{1}{\sqrt{U_{\mathrm{col}}}}\dfrac{\mathrm{d}I_{\mathrm{col}}}{\mathrm{d}U_{\mathrm{col}}}\,\mathrm{d}U_{\mathrm{col}}}. \tag{A6}$$

It should be noted that arbitrary anisotropic distribution functions can be measured using an RFA equipped with two apertures. If the RFA is oriented in some direction $\vec{n}$, it collects from the total anisotropic distribution function only that part of the ions having their velocities inside a cone with a half-angle $\tilde{\theta}_{\mathrm{RFA}} = (D_{\mathrm{ap}}/d_{\mathrm{ap-ER}}) \ll 1$ around the $\vec{n}$ direction. The value of $\tilde{\theta}_{\mathrm{RFA}}$, which is determined only by the RFA geometry, could be chosen small enough so that the ion distribution function may be assumed isotropic for $\tilde{\theta} \leqslant \tilde{\theta}_{\mathrm{RFA}}$ (of course, the decrease in $\tilde{\theta}_{\mathrm{RFA}}$ decreases the collector current as well and hence all of the problems of measuring small currents arise). Thus the distribution function in the vicinity of $\vec{n}$ may be determined using (A5) and the whole anisotropic distribution function may be found by varying the RFA orientation with respect to the plasma source. An additional problem of using the RFA is that it may significantly perturb the plasma due to the shadowing effect of the large RFA body.

References

[1] Boxman R L, Sanders D M and Martin P J (ed) 1995 *Handbook of Vacuum Arc Science and Technology* (Park Ridge, NJ: Noyes)

[2] Beilis I I, Goldsmith S and Boxman R L 2002 *Phys. Plasmas* **9** 3159

[3] Beilis I I, Keidar M, Boxman R L and Goldsmith S 2000 *Phys. Plasmas* **7** 3068

[4] Beilis I I, Boxman R L, Goldsmith S and Paperny V L 1999 *Appl. Phys. Lett.* **75** 2734

[5] Beilis I I, Boxman R L, Goldsmith S and Paperny V L 2000 *J. Appl. Phys.* **88** 6224

[6] Rosenthal H, Beilis I I, Goldsmith S and Boxman R L 1996 *J. Phys. D: Appl. Phys.* **29** 1245

[7] Beilis I I, Boxman R L and Goldsmith S 1999 *J. Phys. D: Appl. Phys.* **32** 128

[8] Beilis I I, Keidar M, Boxman R L, Goldsmith S, Heberlein J and Pfender E 1999 *J. Appl. Phys.* **86** 114

[9] Chen S and Sekiguchi T 1965 *J. Appl. Phys.* **36** 2363

[10] Lochte-Holtgreven W (ed) 1968 *Plasma Diagnostics* (Amsterdam: North-Holland)

[11] Huddlestone R H and Leonard S L (ed) 1965 *Plasma Diagnostic Techniques* (New York: Academic)

[12] Lunev V M, Ovcharenko V D and Khoroshikh V M 1977 *Sov. Phys.—Tech. Phys.* **22** 855

[13] Kutzner J and Miller H C 1989 *IEEE Trans. Plasma Sci.* **17** 688

[14] Lunev V M, Padalka V G and Khoroshikh V M 1977 *Sov. Phys.—Tech. Phys.* **22** 858
[15] Kutzner J and Miller H C 1992 *J. Phys. D: Appl. Phys.* **25** 683
[16] Hutchinson H I 2002 *Principles of Plasma Diagnostics* 2nd edn (New York: Cambridge University Press)
[17] Plyutto A A, Ryzhkov V N and Kapin A T 1965 *Sov. Phys.—JETP* **20** 328
[18] Davis W D and Miller H C 1969 *J. Appl. Phys.* **40** 2212
[19] Kutzner J and Glinkowski M 1983 *IEEE Trans. Plasma Sci.* **PS-11** 233
[20] Rakhovsky V I 1987 *IEEE Trans. Plasma Sci.* **PS-15** 481
[21] Beilis I I, Shashurin A, Nemirovsky A, Goldsmith S and Boxman R L 2004 *Surf. Coat. Technol.* **188–189** 228
[22] Beilis I I, Shashurin A, Nemirovsky A, Goldsmith S and Boxman R L 2005 *IEEE Trans. Plasma Sci.* **33** 1641
[23] Shashurin A, Beilis I I and Boxman R L 2008 *Plasma Sources Sci. Technol.* **17** 015016
[24] Chen F F 1984 *Introduction to Plasma Physics and Controlled Fusion* (New York: Plenum)